Published in "Physical Chemistry Chemical Physics 19 (43): 29271–29277, 2017"
which should be cited to refer to this work.

Distribution of aluminum over different T-sites in ferrierite zeolites studied with aluminum valence to core X-ray emission spectroscopy†

R. Bohinc,[a] J. Hoszowska,[b] J.-Cl. Dousse,[b] W. Błachucki,‡[b] F. Zeeshan,[b] Y. Kayser,§[a] M. Nachtegaal,[a] A. B. Pinar[a] and J. A. van Bokhoven*[ac]

The potential of valence to core Al X-ray emission spectroscopy to determine aluminum distribution in ferrierite zeolites was investigated. The recorded emission spectra of four samples prepared with different structure directing agents exhibit slight variations in the position of the main emission peak and the intensity of its low energy shoulder. Theoretical calculations indicate that an increased intensity of the $K\beta_x$ shoulder in the Al emission spectra can be linked to a predominant occupation of the T3 site by a single aluminum atom. This study thus suggests that valence to core X-ray emission spectroscopy can be applied to help determine the occupation of aluminum at crystallographic T-sites in zeolites.

Zeolites are microporous crystalline aluminosilicates whose frameworks are composed of corner sharing TO_4 tetrahedra (T = either silicon or aluminum). The mutual arrangement of these subunits defines the framework structure which is characterized by periodical pores and channels. Replacing silicon atoms with aluminum atoms at the T-sites introduces a local negative charge to the framework which can be stabilized by protons or cations, which confer the catalytic activity to the zeolite. The catalytic activity is therefore directly related to the positioning of aluminum atoms within the zeolite framework.

The determination of both the location of aluminum atoms at individual T-sites (aluminum sitting) and the mutual arrangement of several aluminum atoms (aluminum distribution) remains an open question in zeolite structural analysis.[1] The Magic Angle Spinning-Nuclear Magnetic Resonance (MAS-NMR) spectroscopy of ^{29}Si represents a standard method to address the Si–Al connectivity, however, not providing information about the absolute position of aluminum and silicon atoms inside the framework. ^{27}Al MAS NMR is sensitive to the averaged Al–O–Si angle and therefore partially yields aluminum occupation.[2,3] Combined with DFT calculations, ^{29}Si and ^{27}Al NMR have been used to study the distribution of aluminum in zeolites ZSM-5[4] (MFI framework type) and ferrierite[5] (FER framework type). Co^{2+} adsorption monitored by UV-visible spectroscopy has been used to study the relative positions of aluminum in zeolites, mainly for ZSM-5 and ferrierite.[5,6] From the amount of adsorbed Co^{2+}, the proportion of ''Al-pairs'', *i.e.* Al–$(O–Si)_2$–Al sequences, where at least one aluminum atom is located in the second coordination shell of another aluminum atom, has been determined. Due to a large penetration depth of X-rays, X-ray-based techniques are suited for the characterization of catalysts under reaction conditions. X-ray absorption fine structure (EXAFS) analysis combined with DFT simulations showed a preference of aluminum for the T sites in the 4-ring of zeolite beta.[7] X-ray absorption near-edge structure spectroscopy (XANES) was successfully applied to monitor aluminum coordination as a function of temperature and gas composition.[8] X-ray diffraction (XRD) techniques are, in general, not suitable for distinguishing silicon and aluminum atoms because of their similar scattering power. The structural changes induced by introducing aluminum, mainly an elongation of the T–O distance by *ca.* 0.1 Å, can in some cases indicate the position of aluminum.[9] However, this difference is obscured by the low Al/Si proportion at that specific T-site. Using the X-ray standing waves, the location of aluminum in scolecite (NAT framework type) has been determined.[10] Although the method yields an absolute occupancy, the dependence of this technique on X-ray photon flux, detector efficiency, and X-ray focusing makes it not applicable for studying nano-sized crystals. Like X-ray absorption spectroscopy, X-ray emission spectroscopy (XES) is an element selective method.[11,12] In this method, the electronic structure of an element can be probed by tunning the energy of the X-rays

[a] *Paul Scherrer Institut (PSI), 5232 Villigen PSI, Switzerland*
[b] *Department of Physics, University of Fribourg, Chemin du Musée 3, CH-1700 Fribourg, Switzerland*
[c] *Department of Chemistry and Applied Biosciences, ETH Zürich, Wolfgang-Pauli-Str. 10, CH-8093 Zürich, Switzerland. E-mail: jeroen.vanbokhoven@chem.ethz.ch*

† Electronic supplementary information (ESI) available. See DOI: 10.1039/c7cp05001a

‡ Current address: Institute of Physical Chemistry of the Polish Academy of Sciences (IPC PAS), ulica Kasprzaka 44/52, 01-224 Warsaw, Poland.
§ Current address: Physikalisch-Technische Bundesanstalt (PTB), Abbestr. 2-12, 10587 Berlin, Germany.

above the associated core ionization threshold. Upon the removal of a tightly bound electron, the inner shell vacancy is filled with an electron from a higher occupied electronic level resulting in the fluorescence of a X-ray photon. By analyzing the chemical shift of the K_α emission lines, core-to-core XES can provide the information about the oxidation state of the probed atom.[13] The chemical sensitivity of the method is, however, higher for valence to core (VtC) transitions. Because occupied electronic valence levels are associated with molecular bonding, VtC XES is sensitive to the local structure around the probed atom. It is particularly well suited for the identification of ligands as it is sensitive to the level of ligand protonation and because it allows ligands with similar atomic numbers to be distinguished.[14] The potential of using VtC XES to study the geometrical structure of molecules containing 3rd row elements (P, S, Cl) in different local symmetries was recently demonstrated.[15,16]

If it is a big challenge to develop tools to locate aluminum in the zeolite, it is even more challenging to synthesize the zeolite with aluminum in specific T positions. The sitting and distribution of aluminum inside the zeolite framework are, however, not random. The group of Dědeček nicely showed that the formation of either Al-pairs or isolated/single aluminum atoms can be promoted by the presence of tetrapropylammonium $(TPA)^+$ and Na^+ cations, and anions in the synthesis mixture.[17] A proven strategy to specifically manipulate the location of aluminum in different T-sites was developed in the laboratory of Prof. Perez-Pariente in Madrid.[18,19] It is based on a rational choice of the structure directing agents (SDAs) according to their interaction with the zeolite framework. A series of samples of zeolite ferrierite was prepared in fluoride medium from gels with very low water content, using different combinations of SDAs: pyrrolidine plus tetramethylammonium (FER-PYRR-TMA), 1-benzyl-1-methylpyrrolidium plus tetramethylammonium (FER-BMP-TMA) and pyrrolidine (FER-PYRR).[19,20] The gel composition was $0.969SiO_2/0.031Al_2O_3/x$SDA1/$(0.54 - x)$SDA2/$0.48HF/4.65H_2O$, where x was 0.06 for syntheses with two SDAs (FER-BMP-TMA and FER-PYRR-TMA) and 0 for those with only one SDA (FER-PYRR). The fourth sample (FER3) was synthesized using the conventional procedure in alkaline medium and in the presence of sodium.[19] The samples had a similar Si/Al ratio but a different proportion of Brønsted sites located in the 10-ring or in the less accessible cage, as determined using FTIR-monitored pyridine adsorption.[21] Pyridine is too bulky to access the ferrierite cavity passing through the 8-ring window, and therefore cannot be protonated by the acid sites located within the cavity. The sample FER-PYRR has the lowest percentage of accessible acid sites (only 10 percent), which suggests that 90 percent of the acid sites are in not accessible locations within the cavity. When TMA was added to the gel, the percentage of accessible sites increased to 18 percent, and a further increase to 36 percent was found in the sample FER-BMP-TMA. In all of these cases the percentage of accessible sites is lower than that of a conventional ferrierite (*ca.* 50 percent). A detailed structure analysis allowed understanding the influence of SDA on the distribution of acid sites.[22] In the sample FER-PYRR, the shortest N–O distance between pyrrolidine and a framework oxygen atom occurs with an oxygen bonded to the T3 site only, which suggests that aluminum must be preferentially located at that site. That oxygen bonded to T3 is located in the ferrierite cavity, and the associated Brønsted site would not be accessible to relatively bulky molecules, which explains the low percentage of acid sites accessible to pyridine. Co^{2+} adsorption experiments performed on the same FER-PYRR sample showed constant isosteric heats obtained for Co^{2+} coverage up to 1, something rarely observed in zeolites. This indicates that most of the aluminum is at the same T position.[23] Differences in the distribution of aluminum as a function of the SDA used in the syntheses were confirmed by ^{27}Al Multiple Quantum (MQ) MAS NMR.[18] These differences have a strong impact on the catalytic performance of the samples as they exhibit significantly higher selectivity to isobutene and higher resistance to deactivation than the conventional ferrierite.[24] Molecular simulation showed that the probability of the occupation of specific T-sites by aluminum changes when the SDAs are introduced.[22]

In this study we explore the potential of Al VtC XES to determine the distribution of aluminum atoms in the zeolite framework. The ferrierite samples prepared with different SDAs[20] exhibit a different positioning of aluminum inside the framework and thus represent an ideal set of samples to study the sensitivity of the technique to aluminum siting and distribution.

The Al VtC XES measurements were performed at the SLS PHOENIX I beam line. The energy of the incoming photon beam was tuned to 2.5 keV using a Si(111) monochromator and the photon flux was approximately 9×10^{11} photons per s. The VtC X-ray emission spectra were measured in high energy resolution using the von Hamos X-ray spectrometer of Fribourg[25] equipped with an ADP(101) crystal ($2d$ = 10.642 Å) bent cylindrically to a radius of 25.4 cm. With this crystal, the energy range covered by the spectrometer for a fixed position of the crystal and detector was 41 eV. The diffracted X-rays were measured with a back-illuminated CCD detector.[26] The spectrometer was operated in the so-called slit geometry. In this geometry, a narrow rectangular slit, placed between the sample and the crystal, serves as the effective source of radiation. A slit width of 0.15 mm was adopted as the best compromise between a high enough energy resolution and an acceptable spectrometer efficiency. The measurements were performed under ambient temperature at a pressure of about 10^{-6} mbar.

The energy calibration of the spectrometer was performed by measuring the Kα diagram X-ray lines from aluminum and by assigning to these reference lines the energies reported in ref. 27 (see Fig. S1, ESI†). These calibration measurements were also used to determine the instrumental broadening of the spectrometer. The instrumental response of the latter was found to be well reproduced by a Lorentzian function with a FWHM varying between 0.27 eV at 1.487 keV. For each sample, the average measuring times of the Al VtC XES spectra was approximately 17 h.

The background subtracted Al VtC emission spectra of the ferrierite samples are shown in Fig. 1. The background subtraction of the measured spectra is explained in detail in the ESI† (see Sections VI and VII). Two features can be resolved in the experimental spectra; the stronger feature ($K\beta_{1,3}$) located at

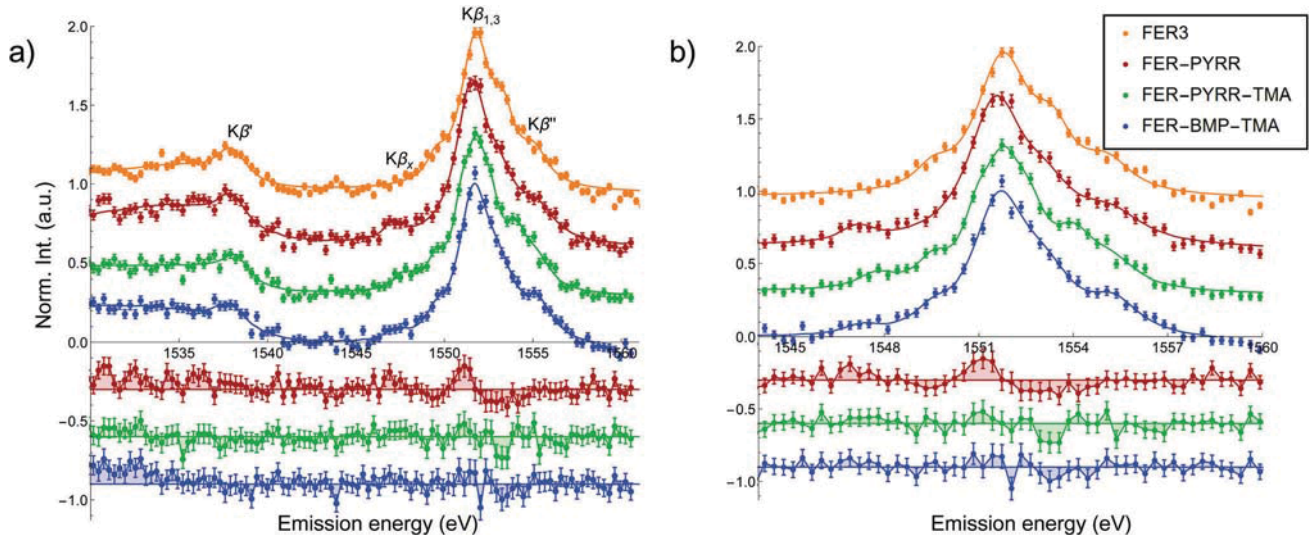

Fig. 1 (a) Background subtracted experimental Al VtC emission spectra of FER-BMP-TMA, FER-PYRR-TMA, FER-PYRR and FER3 samples. (b) Zoom in of the main emission peak. The full lines represent the fitted functions. The difference spectra correspond to differences with respect to the spectrum of FER3. See main text for labeling of the observed features.

1552 eV with low ($K\beta_x$) and high ($K\beta''$) energy shoulders, and a weaker feature ($K\beta'$) located approximately 14 eV below $K\beta_{1,3}$. We notice that the emission spectra exhibit a very broad and asymmetric $K\beta'$ feature extending more than 10 eV towards lower energies. The differences observed in the spectra measured for the four studied samples are subtle and feature a blue shift of the $K\beta_{1,3}$ in the FER3 sample and a decreased $K\beta_x$ shoulder with respect to other samples, best observed when comparing to the FER-PYRR sample (see Fig. 1b). Also differences in the height of the $K\beta'$ are found. Because of the limited energy range covered by the CDD detector the differences in the intensity of the Al $K\beta'$ feature could be an artefact caused by background subtraction and we therefore focus our analysis on the main peak (see Fig. 1b). In addition to Al VtC XES spectra also Si VtC XES spectra were measured (see Fig. S2, ESI†).

To obtain information about the positioning of aluminum atoms within the framework we simulate Al XES spectra with DFT as described previously.[16] The ferrierite framework[28] is composed of 10-ring and 8-ring channels that run perpendicular to each other. There are also 6-ring channels parallel to the 10-ring channels, whose intersection with the 8-ring channels forms the so-called FER cavities, accessible only through the 8-ring windows (Fig. 2). There are four non-equivalent T positions in the FER structure, which we label T1–T4. The T2 and T4 positions are located in the flat 6-ring (β-sites), while the T1 and T3 positions are found in the twisted 6-ring composed of two 5-rings (α-sites). The α- and β-sites restrict the FER cavity from perpendicular directions and represent sites for accommodation of bare divalent cations.[1,29] Our model structure is composed of α- and β-sites containing silicon/aluminum atoms forming the two 6-rings and O atoms connected to the T-sites, shown in Fig. 2(b) and (c). To compensate for the lack of positive charge around oxygen atoms at the border of the model structures, positive point charges located at T-sites from the second

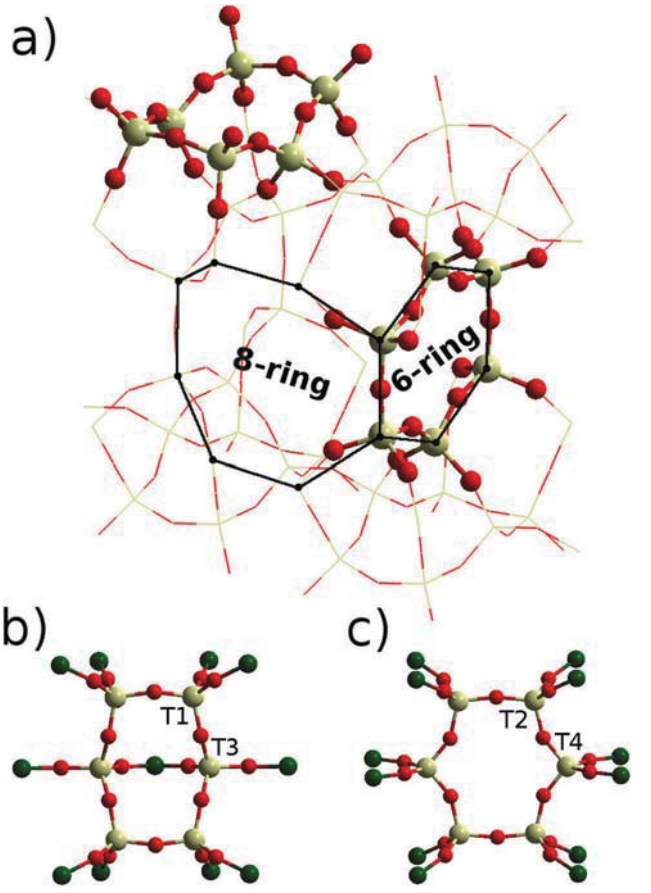

Fig. 2 Structure of the ferrierite framework with oxygen and Si/Al atoms in red and yellow colors. The green spheres represent point charges implemented in the model α- and β-sites. (a) Periodic building unit with α- and β-sites represented by spheres. The 6-ring and 8-ring confine the FER cavity. (b) Model of the α-site containing T_1 and T_3 positions. (c) Model of the β-site with T_2 and T_4 positions.

coordination shell around α- and β-sites have been included. These neutral structures represent a minimal model for addressing aluminum distribution in Si-rich ferrierite zeolites as 97% of aluminum in such zeolites is located in single Al and Al–O–$(Si–O)_2$–Al sequences.[1] Due to the Loewenstein rule, *i.e.* two aluminum atoms can not share a common oxygen atom, the smallest structure that can accommodate an Al–O–$(Si–O)_2$–Al sequences is, namely, a 6-ring.

There are 12 possible aluminum occupations in our model structures that can be divided into three groups: single aluminum atoms (T1, T2, T3 and T4), Al–O–(Si–O)–Al sequences (T11s, T13s, T22s, and T24s) and Al–O–$(Si–O)_2$–Al sequences (T11, T22, T33, and T44) (see Fig. S3, ESI†). For each of the corresponding occupations, VtC XES spectra were computed using the frozen ground state DFT approach implemented in the StoBe program package,[30] yielding approximate oscillator strengths and emission energies. The orbital basis in the XES calculations for Al and Si were (6321/521/1) while for O the (5211/411/11) basis was employed. Our calculations indicate that the inclusion of polarization functions on all atoms is necessary to correctly describe the electronic structure of the ferrierite framework. An augmentation of the chosen basis sets showed no significant improvement of emission spectra. For the exchange and correlation functionals, PD86[31] and PBE[32] functionals were chosen. The theoretical spectra were built from the calculated stick spectrum using Voigt profiles. The Lorentzian width was set to 0.47 eV to describe the Al-K line width,[33] while the Gaussian width was set to 1.5 eV to take into account the combined effect of experimental broadening and compensation for the size-limitation of our model. The computed emission spectra were shifted by 55.5 eV to match the experimental peak position of the $K\beta_{1,3}$ features.

The theoretical Al VtC XES spectra corresponding to different occupations of α- and β-sites are shown in Fig. 3. The subtle differences in the computed spectra indicate variations in the geometrical structure of the T-sites as well as differences in the electronic structure caused by Al–Al and Al–Si interactions (see for example the T33–T3 difference spectrum). This suggests that VtC XES is not only sensitive to aluminum sitting but also to aluminum distribution. An inspection of the molecular origin of emission lines shows that the Kβ′ feature corresponds to electronic transitions from valence orbitals with a strong contribution from Al(3p) and O(2s) atomic components to the Al(1s) orbital. The main peak, composed of $K\beta_{1,3}$, $K\beta_x$, and Kβ″

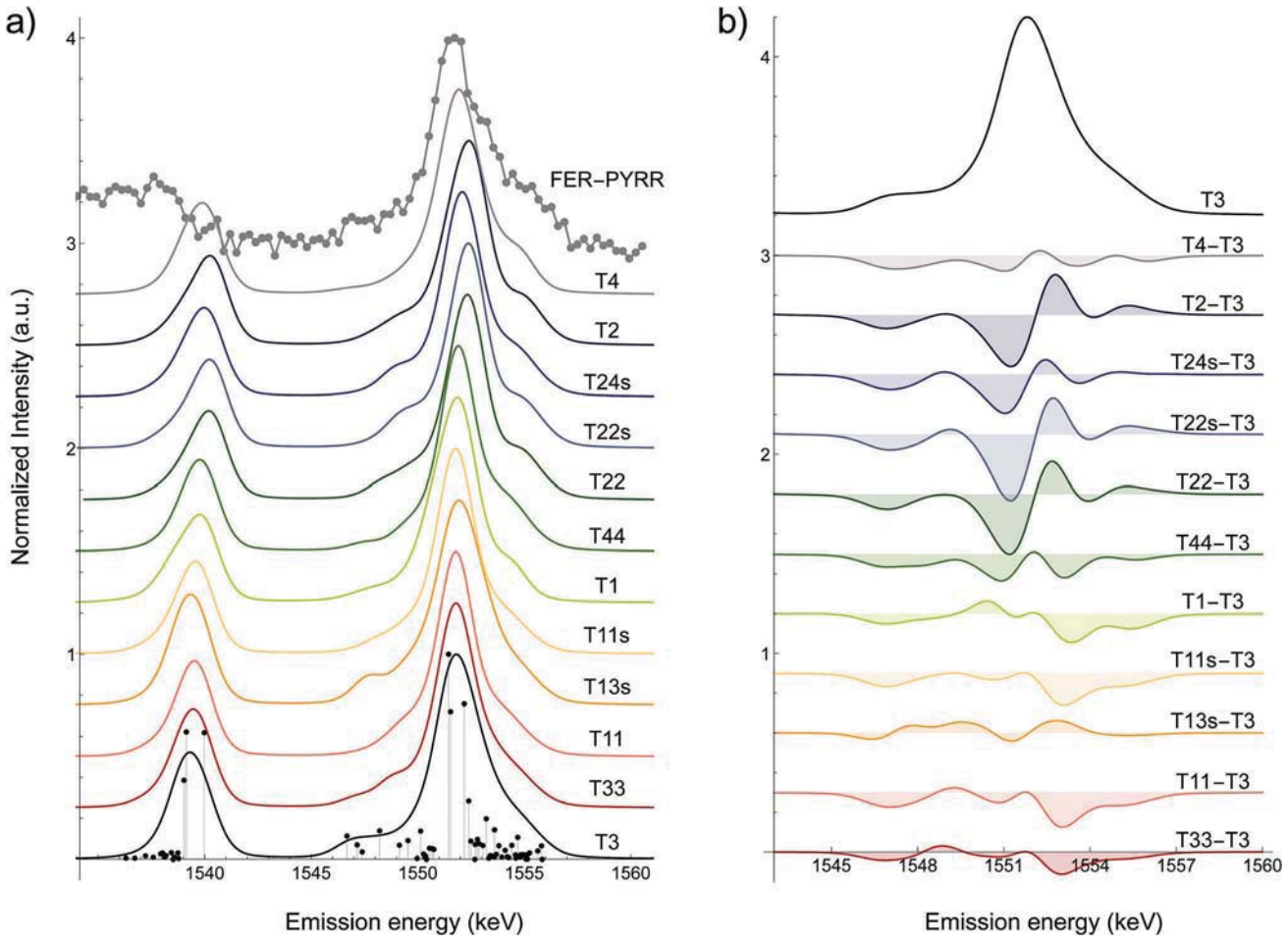

Fig. 3 (a) Comparison between theoretical Al VtC spectra for aluminum occupying different α-site and β-site configurations. The experimental spectra of the FER-PYRR sample are appended. (b) The corresponding difference spectra with respect to the emission spectrum of the T3 site shown at the top.

features, corresponds to transitions from the Al(3p)O(2p) valence orbitals with σ, σ/π, π characters, respectively, to the Al(1s) orbital. A shift of approximately 0.4 eV in the position of the $K\beta_{1,3}$ feature is found between α- and β-site occupation for both spectra. Emission spectra corresponding to the occupation of α-sites model better the $K\beta_x$ feature, while spectra corresponding to the occupation of β-sites model better the Kβ″ feature. The calculated energy difference between Kβ′ and $K\beta_{1,3}$ is approximately 2 eV too small in comparison with experimental spectra and is attributed to the limitations of the model. The strongly asymmetric shape of the Kβ′ peak in the Al emission spectra is not reproduced by our calculations. To verify that the observed discrepancy is not caused by an insufficient size of our model, T-sites corresponding to the second coordination shell of the 6-rings were included, but the Kβ′ peak of the calculated spectra showed no substantial differences with regards to the one from our model (see Fig. S4, ESI†). The origin of the shape of the experimental Kβ′ peak is therefore not fully understood. However, because of the limited energy range in the experimental Al VtC emission spectra, the broad and asymmetric shape of the Kβ′ feature might be caused by wrong background subtraction.

To obtain the relative occupation of aluminum configurations in the measured samples, we fit the main peak of the experimental spectra containing features $K\beta_{1,3}$, Kβ′, and $K\beta_x$ with a linear combination of the calculated spectra (see Section V of the ESI† for details). The fitted spectra reproduce all the features and model the variations in the intensity of the $K\beta_x$ feature and the shift of the $K\beta_{1,3}$ peak (see Fig. S5, ESI†). The variations of the Kβ″ feature are, on the other hand, not reproduced. The quality of the fit, estimated by a reduced χ^2 value of 4, suggests that the theoretical model is not fully optimized. An additional augmentation of the employed model with respect to the model size was, however, not possible due to problems with convergence of the associated wave function. The computation of more accurate spectra likely requires the application of more accurate methods than the one employed in this work. The resulting concentrations of T-sites for different samples are shown in Fig. 4.

Our analysis indicates a significant population of the T3, T22s, T13s, and T24s configurations in our samples. Due to the similarity of the numerous theoretical spectra, the fitting errors of the obtained concentrations are as high as 25% and the determination of most concentrations remains within this uncertainty. Despite this high uncertainty, the analysis suggests that the T3 position is preferably occupied in all the samples. The distribution of aluminum in FER-PYRR, FER-BMP-TMA, and FER-PYRR-TMA samples is clearly different from that of the FER3 sample. An inspection of the experimental spectra (see Fig. 5) reveals that the emission spectra of FER-PYRR, FER-BMP-TMA, and FER-PYRR-TMA samples exhibit a larger $K\beta_x$ shoulder than that of the FER3 sample. We notice the $K\beta_x$ feature is only present in the theoretical spectra corresponding to the T3 and T13s configurations. The spectrum of the T13s configuration, however, exhibits a blue shift of the $K\beta_x$ feature with respect to the experimental spectra and we can therefore link a high intensity of the $K\beta_x$ shoulder to an increased concentration of single aluminum atoms occupying the T3 site. Additionally, as

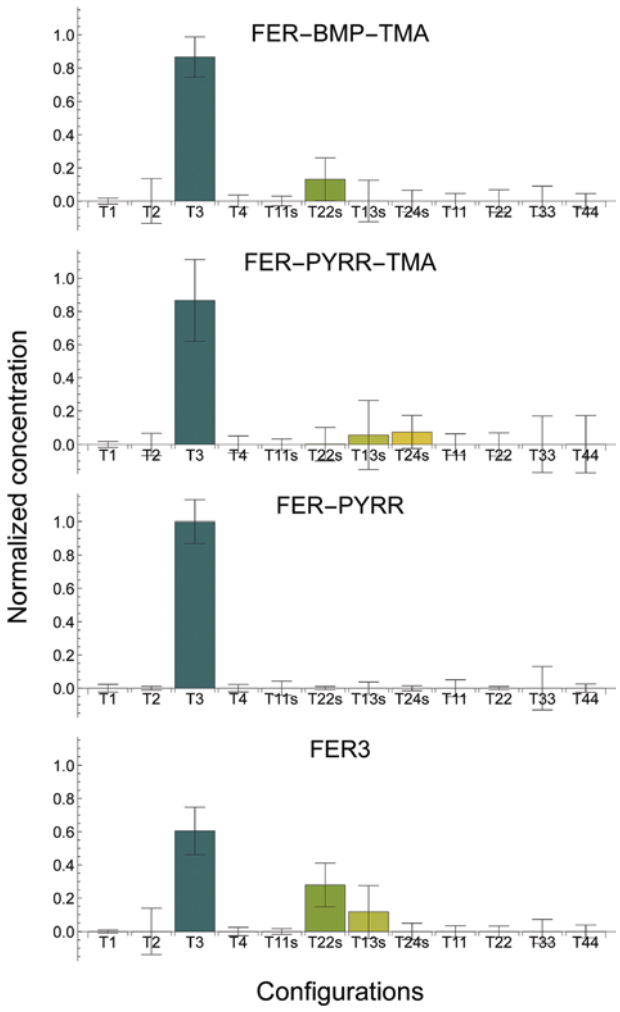

Fig. 4 Normalized concentration of different aluminum configurations obtained in the fit of Al VtC emission spectra of FER-BMP-TMA, FER-PYRR-TMA, FER-PYRR samples. See text for the labeling of configurations.

the $K\beta_{1,3}$ peak of the FER3 sample is slightly blue shifted with respect to those from the other samples (see Fig. 1b), a decreased population of α-site configurations (see Fig. 3), including the T3 configurations, is expected for this sample.

The highest and lowest concentration of aluminum in the T3 site is found for the FER-PYRR and FER3 samples, respectively. This is in agreement with the results from previous studies.[21,22,24,34] In particular, FTIR-monitored pyridine adsorption showed that the lowest and highest percentages of accessible acid sites also correspond to FER-PYRR and FER3 samples.[21] A Brønsted site associated to aluminum in T3 is not accessible, since the four oxygen atoms bonded to it point to the inner part of the cavity. This is also reflected in the very low catalytic activity of the FER-PYRR sample for *m*-xylene and *n*-butene isomerization, as explained elsewhere.[24] T3 was also the most favorable location for aluminum for the FER-PYRR sample found in our X-ray diffraction[22] and molecular simulation studies.[34] These studies, however, report also that the most occupied configuration for FER-PYRR-TMA was T1 and for FER-BMP-TMA and FER3 it was T2 and thus deliver results divergent to our present findings

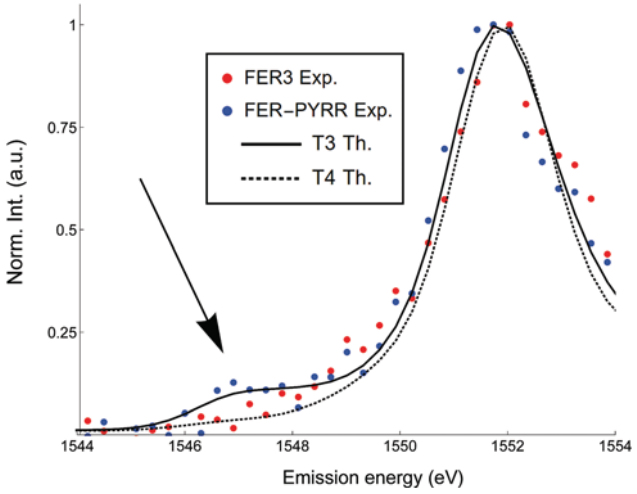

Fig. 5 A comparison between the experimental emission spectra of the FER-PYRR (blue dots) and FER3 (red dots) samples focused on the $K\beta_x$ feature (indicated with an arrow) together with the theoretical spectra corresponding to the T3 (black full line) and T4 (black dotted line) configurations.

which indicate higher occupancy of configurations different than T1 and T2. This discrepancy can be explained by the fact that the VtC X-ray emission spectra calculated on the basis of the applied model allow to efficiently distinguish only samples of an increased T3 and T13s configurations population.

In summary, in this study we have investigated the possibility of using Al VtC XES spectroscopy to determine aluminum distribution in the zeolite framework. The Al VtC spectra of four samples with a similar Si/Al ratio but different aluminum distribution indicate minor differences in the intensity and position of $K\beta_x$ and $K\beta_{1,3}$ features, respectively. As indicated by our theoretical calculations, an increased intensity of the $K\beta_x$ in the Al VtC emission spectra can be linked to a higher occupation of the T3 site by a single aluminum atom. The maximal and minimal occupation of the T3 site by aluminum was observed in the FER-PYRR and FER3 samples, respectively, which confirms the results from previous works.[21,22,34] Because the electronic transition from valence to core levels has a low probability, VtC XES requires a high photon flux especially when applied to study aluminum distribution in samples with low aluminum concentration. Adaptation of the described methodology at high brilliance X-ray sources under resonant conditions has a high potential to increase the technique's sensitivity to the electronic and geometrical structure of aluminum centers in zeolites. These improvements can potentially allow *in situ* characterization of zeolite materials.

Conflicts of interest

There are no conflicts to declare.

Acknowledgements

The research leading to these results has received funding from the European Community's Seventh Framework Program (FP7/2007-2013) under grant agreement no. 290605 (COFUND: PSI-FELLOW). Four of us (J. H, J.-Cl. D. W. B. and F. Z.) acknowledge the financial support of the Swiss National Science Foundation *via* the grant 200020-146739. Prof. Joaquín Pérez-Pariente, from the Institute of Catalysis and Petroleum Chemistry, CSIC (Spain) is gratefully acknowledged for developing the synthesis strategy to control the aluminum distribution in zeolite ferrierite. We thank SLS for the provision of beamtime at the Phoenix beamline. A. B. P. thanks the Energy System Integration (ESI) platform at Paul Scherrer Institute for funding.

References

1 J. Dědeček, Z. Sobalík and B. Wichterlová, *Catal. Rev.*, 2012, **54**, 135–223.
2 E. Lippmaa, A. Samoson and M. Magi, *J. Am. Chem. Soc.*, 1986, **108**, 1730–1735.
3 S. H. Kable, W. D. Lawrance and A. E. W. Knight, *J. Phys. Chem.*, 1982, **86**, 1244–1247.
4 J. Dědeček, S. Sklenak, C. Li, B. Wichterlová, V. Gábová, J. Brus, M. Sierka and J. Sauer, *J. Phys. Chem. C*, 2009, **113**, 1447–1458.
5 J. Dědeček, M. J. Lucero, C. Li, F. Gao, P. Klein, M. Urbanova, Z. Tvaruzkova, P. Sazama and S. Sklenak, *J. Phys. Chem. C*, 2011, **115**, 11056–11064.
6 J. Dědeček, V. Balgová, V. Pashkova, P. Klein and B. Wichterlová, *Chem. Mater.*, 2012, **24**, 3231–3239.
7 A. Vjunov, J. L. Fulton, T. Huthwelker, S. Pin, D. Mei, G. K. Schenter, N. Govind, D. M. Camaioni, J. Z. Hu and J. A. Lercher, *J. Am. Chem. Soc.*, 2014, **136**, 8296–8306.
8 J. A. van Bokhoven, A. M. van der Eerden and D. C. Koningsberger, *J. Am. Chem. Soc.*, 2003, **18**, 7435–7442.
9 A. Alberti, P. Davoli and G. Vezzalini, *Z. Kristallogr. – Cryst. Mater.*, 1986, **175**, 249–256.
10 J. A. van Bokhoven, T.-L. Lee, M. Drakopoulos, C. Lamberti, C. Thiess and J. Zegenhagen, *Nat. Mater.*, 2008, **7**, 551–555.
11 P. Glatzel, R. A. Mori and D. Sokaras, in *X-Ray Absorption and X-Ray Emission Spectroscopy: Theory and Applications*, ed. J. A. van Bokhoven and C. Lamberti, John Wiley & Sons, West Sussex, 2016, ch. 6, vol. 1, pp. 125–149.
12 P. Glatzel and U. Bergmann, *Coord. Chem. Rev.*, 2005, **249**, 65–95.
13 R. A. Mori, E. Paris, G. Giuli, S. G. Eeckhout, M. Kavčič, M. Žitnik, K. Bučar, L. G. M. Pettersson and P. Glatzel, *Inorg. Chem.*, 2010, **49**, 6468–6473.
14 G. Smolentsev, A. V. Soldatov, J. Messinger, K. Merz, T. Weyhermüller, U. Bergmann, Y. Pushkar, J. Yano, V. K. Yachandra and P. Glatzel, *J. Am. Chem. Soc.*, 2009, **131**, 13161–13167.
15 M. Petric, R. Bohinc, K. Bučar, S. H. Nowak, M. Žitnik and M. Kavčič, *Inorg. Chem.*, 2016, **55**, 5328–5336.
16 M. Petric, R. Bohinc, K. Bučar, M. Žitnik, J. Szlachetko and M. Kavčič, *Anal. Chem.*, 2015, **87**, 5632–5639.
17 V. Pashkova, P. Klein, J. Dědeček, V. Tokarová and B. Wichterlová, *Microporous Mesoporous Mater.*, 2015, **202**, 138–146.

18 A. B. Pinar, R. Verel, J. Pérez-Pariente and J. A. van Bokhoven, *Microporous Mesoporous Mater.*, 2014, **193**, 111–114.
19 A. B. Pinar, PhD thesis, Madrid, 2010.
20 A. B. Pinar, L. Gomez-Hortiguela and J. Pérez-Pariente, *Chem. Mater.*, 2007, **19**, 5617–5626.
21 A. B. Pinar, C. Márquez-Álvarez, M. Grande-Casas and J. Pérez-Pariente, *J. Catal.*, 2009, **263**, 258–265.
22 A. B. Pinar, L. Gómez-Hortigüela, L. B. McCusker and J. Pérez-Pariente, *Chem. Mater.*, 2013, **25**, 3654–3661.
23 P. Nachtigall, L. Grajciar, J. Perez-Pariente, A. B. Pinar, A. Zukal and J. Cejka, *Phys. Chem. Chem. Phys.*, 2012, **14**, 1117–1120.
24 C. Márquez-Alvarez, A. B. Pinar, R. García, M. Grande-Casas and J. Pérez-Pariente, *Top. Catal.*, 2009, **52**, 1281–1291.
25 J. Hoszowska, J.-C. Dousse, J. Kern and C. Rhême, *Nucl. Instrum. Methods Phys. Res., Sect. A*, 1996, **376**, 129–138.
26 J. Szlachetko, *et al.*, *Rev. Sci. Instrum.*, 2007, **78**, 093102.
27 R. D. Deslattes, *et al.*, *Rev. Mod. Phys.*, 2003, **75**, 35–99.
28 P. Vaughan, *Acta Crystallogr.*, 1966, **21**, 983–990.
29 J. Dědeček, D. Kaucký and B. Wichterlová, *Microporous Mesoporous Mater.*, 2000, **35**(6), 483–494.
30 K. Hermann, L. G. M. Pettersson, M. E. Casida, C. Daul, A. Goursot, A. Koester, E. Proynov, A. St-Amant, D. R. Salahub, V. Carravetta, H. Duarte, C. Friedrich, N. Godbout, J. Guan, C. Jamorski, M. Leboeuf, M. Leetmaa, M. Nyberg, S. Patchkovskii, L. Pedocchi, F. Sim, L. Triguero and A. Vela, *StoBe-deMon*, 2014.
31 J. P. Perdew, *Phys. Rev. B: Condens. Matter Mater. Phys.*, 1986, **33**, 8822–8824.
32 J. P. Perdew, K. Burke and M. Ernzerhof, *At. Data Nucl. Data Tables*, 1996, **77**, 3865–3868.
33 J. A. Campbell and T. Papp, *At. Data Nucl. Data Tables*, 2001, **77**, 1–56.
34 L. Gómez-Hortigüela, A. B. Pinar, F. Coràb and J. Pérez-Pariente, *Chem. Commun.*, 2010, **46**, 2073–2075.